An observational study of turbulence inside a closed basin

Peijian Fu,[1] Shiyuan Zhong,[2] C. David Whiteman,[3] Tom Horst,[4] and Xindi Bian[5]

Received 11 April 2010; revised 27 July 2010; accepted 14 September 2010; published 15 December 2010.

[1] Data from a flux tower on the floor of Arizona's Meteor Crater are compared to data on the plain outside the crater to determine the impact of basin topography on surface-layer mean and turbulence properties, focusing particularly on windy periods. The bowl-shaped crater amplifies the diurnal oscillations of temperature and heat fluxes, with the amplification most pronounced under quiescent synoptic conditions. The crater's rim shelters the crater atmosphere from mean background flows so that wind speeds inside the crater are usually less than half the speeds on the outside plain. But flows in the crater are much more turbulent, with turbulence presumably generated by the conversion of mean flow into turbulent motion. On days with near-surface winds outside the crater greater than 10 m s^{-1}, turbulent kinetic energy can reach extremely large values (~15 m^2 s^{-2}) inside the crater. Compared to the velocity and temperature spectra outside, spectral peaks occur at lower frequencies inside the crater, especially for the cross-stream wind component. The surface layer is very shallow (<2 m) on the crater floor, suggesting that the similarity theory-based empirical formulas may not be useful for describing properties of the flow at that location.

Citation: Fu, P., S. Zhong, C. D. Whiteman, T. Horst, and X. Bian (2010), An observational study of turbulence inside a closed basin, *J. Geophys. Res.*, *115*, D23106, doi:10.1029/2010JD014345.

1. Introduction

[2] Many major population centers in the western United States, such as Salt Lake City, Las Vegas, Reno, and Los Angeles, are located in close proximity to complex terrain. Many of these areas suffer from poor air quality caused, in part, by rapid growth of population and by the meteorological conditions unique to their topography. Forecasting weather and air quality using atmospheric numerical models is challenged by orographic gradients that require high resolution and by conditions in the atmospheric boundary layer that are often in violation of the assumptions made in developing model physical parameterizations.

[3] One source of errors for model forecasting over complex terrain is the poor description of turbulent mixing. The surface layer turbulence parameterizations commonly used in atmospheric numerical models are principally based on the Monin-Obukhov similarity theory (MOST; see *Monin and Obukhov* [1954]), which assumes horizontal homogeneity and local equilibrium, conditions that are clearly violated in complex terrain. These parameterizations have been developed using data from observational studies over generally flat terrain [*Businger et al.*, 1971; *Wyngaard and Coté*, 1971; *Nieuwstadt*, 1984; *Sorbjan*, 1986; *Mahrt et al.*, 1998] and have been shown to be valid in the case of horizontal homogeneity [*Kaimal and Finnigan*, 1994].

[4] There is a lack of both turbulence theory and observational data that properly describe the turbulence structure over uneven terrain. Compared to studies in flat terrain, relatively few studies have examined turbulence structures in complex terrain. *Kaimal et al.* [1982] examined the spectral behavior of wind velocity and temperature for turbulence data taken at the 300 m tower of the Boulder Atmospheric Observatory and found that, except for minor shifts in the vertical velocity and temperature spectral peaks, the gently rolling terrain at the site does not seem to affect the turbulence spectra in any perceptible manner. *Mengesha et al.* [2001] analyzed data from National Center for Atmospheric Research (NCAR) Queen Air boundary layer flights over the Nebraska Sandhills to study the effects of these low hills on boundary layer turbulence. They noticed that the hills exert their biggest impact on early morning flight data, where horizontal velocity perturbations appear at the same wavelengths as the terrain and the normalized variances are significantly enhanced relative to standard flat terrain data; by contrast the vertical velocity variance seems less affected and terrain effects are much less evident in data from flights in the afternoon convective boundary layer. *Monti et al.* [2002] analyzed measurements collected at a slope site by the Vertical Transport and Mixing Experiment (VTMX) conducted in the Salt Lake Valley in October

[1]Key Laboratory of Semi-Arid Climate Change of the Education Ministry, College of Atmospheric Sciences, Lanzhou University, Lanzhou, China.
[2]Department of Geography, Michigan State University, East Lansing, Michigan, USA.
[3]Department of Atmospheric Sciences, University of Utah, Salt Lake City, Utah, USA.
[4]National Center for Atmospheric Research, Boulder, Colorado, USA.
[5]Northern Research Station, U.S. Department of Agriculture Forest Service, East Lansing, Michigan, USA.

0148-0227/10/2010JD014345

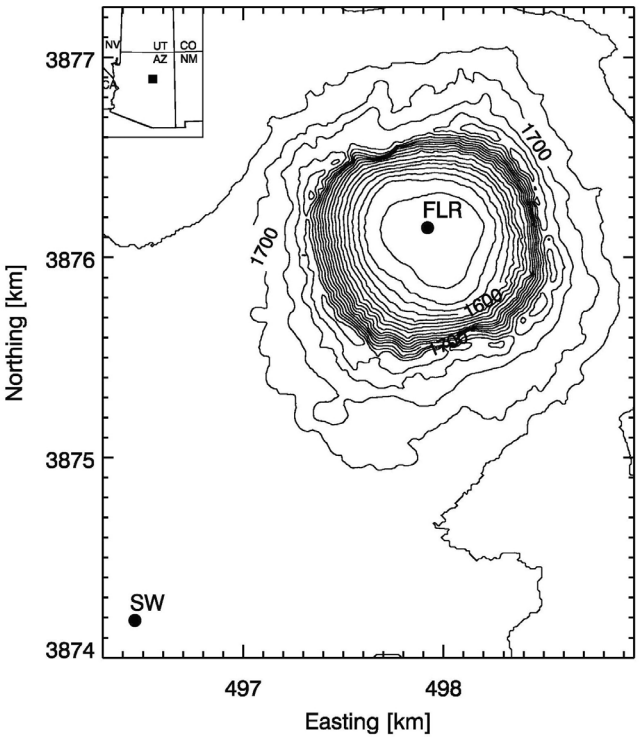

Figure 1. Universal Transverse Mercator zone 12S topographic map of the Arizona's Meteor Crater and environs, indicating the locations of the two flux towers at FLR and SW. Contour interval is 10 m. The inset shows the location of the topographic map in Arizona. Map provided by S. W. Hoch.

2000. Their results show that, although turbulence was generally weak and continuous, sudden increases of turbulence levels occurred as the mean gradient Richardson number dropped to about unity. *Princevac et al.* [2008] also showed that along-slope flow oscillations are associated with fluctuations of the local gradient Richardson number, which appears to vary mostly in the range between 0.25 and 1, leading the authors to conclude that turbulence generation is mainly related to nonlinear instabilities. The Riviera Project [*Mathias et al.*, 2004] collected an extensive turbulence data set in an Alpine valley to help improve turbulence schemes in meteorological and hydrological numerical models. More recently, *Martins et al.* [2009] made observations over the mountainous region of Serra Geral in southern Brazil using a 15 m micrometeorological tower located at the edge of a sharp cliff. They found that the normalized standard deviations of the vertical velocity component and temperature follow Monin-Obukhov similarity for all stability regimes, regardless of the wind direction.

[5] While some observational studies of turbulence properties have been conducted over isolated two-dimensional slopes [*Horst and Doran*, 1988], gently sloped terrain [*Whiteman and Zhong*, 2008], and inside large valleys [*Rotach et al.*, 2004; *Coulter and Doran*, 2002; *Monti et al.*, 2002], few studies have been carried out in basins. The METCRAX experiment in Arizona's Barringer or Meteor Crater [*Whiteman et al.*, 2008] provides a rich data set for understanding turbulence structure inside a small basin. In this study, we analyze METCRAX turbulence data to investigate turbulence structure inside the crater, in particular emphasizing windy periods. By comparing data inside the crater with observations over the plain outside the crater, we investigate how the basin topography modifies turbulence properties and whether theories derived using data over flat terrain are still valid inside a small closed basin.

2. Data and Methods

2.1. Observational Sites and Instrumentation

[6] Data in this study come from the METCRAX experiment conducted in the Meteor Crater ~40 km east of Flagstaff, Arizona [*Whiteman et al.*, 2008]. Meteor Crater was formed by a meteorite impact about 49,000 years ago and is one of the most well-preserved craters in the world. The bowl-shaped crater is about 1.2 km in diameter at the rim level and 165 m deep with a rim 30–60 m above the level of the surrounding plain of the Colorado Plateau (Figure 1). The crater floor and walls are sparsely covered by grasses and bushes. Unlike many other small basins of similar size that have varying ridgeline heights and major passes, the Meteor Crater ridgeline is unbroken by major saddles or passes and is nearly uniform in height, thus reducing the effects of advection and simplifying the physical understanding of the mass, momentum, and energy budgets inside the crater.

[7] The METCRAX experiment was conducted in October 2006 during which continuous measurements of meteorological variables, turbulence fluxes, and radiative and soil fluxes were made inside the crater and immediately outside with an array of micrometeorological flux towers, the Integrated Surface Flux System operated by NCAR's Earth Observing Laboratory (EOL). Inside the crater, there were 5 flux towers located on an east-west transect with one tower on the center floor and two on the eastern sidewall and two on the western sidewall. There was also a tower on the rim of the crater and another one about 1.8 km to the southwest of the crater to capture the background conditions. Because the prevailing wind direction during the period of observation was southwest, the southwest tower was upstream of the crater and was nearly unaffected by the crater on most days. The southwest tower was also located over the nearly flat plain of the Colorado Plateau, making its measurements ideal for comparison with those inside the crater to understand the terrain effect.

[8] In this paper, we compare turbulence measurements inside and outside the crater using data from the tower on the crater floor (FLR) and the tower on the plain to the southwest of the crater (SW) (Figure 1). The following paragraph describes the measurements from these two towers. Detailed descriptions of other METCRAX measurements and analyses are given by *Whiteman et al.* [2008] and *Yao and Zhong* [2009].

[9] The FLR tower was 9 m tall. Measurements of temperature, relative humidity and three-dimensional (3D) wind components were made at four levels (0.5, 2, 5 and 8.5 m) using mechanically aspirated hygrothermometers and 3D sonic anemometers. The same instruments were also used on the SW tower with the hygrothermometer at a height of 2 m and 3D sonic at 3 m. The FLR tower was located near

Table 1. Characteristics of the Two Observational Sites

Site Name	ID	Latitude (°W)	Longitude (°N)	Altitude (m MSL)	Slope Angle (deg)
Crater floor	FLR	111.0225	35.0280	1563	–
Southwest	SW	111.0388	35.0103	1697	2

the center of the crater floor, a flat area ~150–200 m in radius surrounded by sloping sidewalls. The sidewalls increase in slope angle with altitude, culminating in steep cliffs just below the crater rim on the northwest and south walls (see Figure 1). The SW tower was located over a plain that sloped gently upward (~2° slope) on the regional (~50 km) scale toward the southwest. Additional geographic information on the FLR and SW tower sites is provided in Table 1. Campbell Scientific Inc. CSAT3 sonic anemometers were used for turbulence measurements. The sampling frequency of the sonic anemometers was 60 Hz with three sample averages output at 20 Hz. The full data set from each tower was stored on a 60 GB hard drive that was downloaded manually at about weekly intervals. The FLR tower collected good data from the beginning to the end, but sonic data were missing at the SW site for the first 8 days of the experiment. Consequently, data from 9–30 October are used for our analyses.

2.2. Data Processing Method

[10] Sonic anemometer data were rotated into a flow-normal coordinate system using the planar fit technique [*Wilczak et al.*, 2001]. The rotation was accomplished using the mean flow directions determined from 5 min average wind data for the entire project. The data were then rotated into a flow-parallel geographic coordinate system with a project-average vertical velocity of zero and with the u component positive for flows from west to east and the v component positive for flows from south to north. Following rotation of the sonic data to a flow-normal coordinate system, tilt calculations were repeated and residual lean angles were 0.1 degree or less, confirming the success of the coordinate rotation. The scatter about the elevation angle axis was identical to the root mean square residual found initially and the scatter was symmetric about the elevation axis.

3. Results and Discussion

3.1. Mean and Turbulence Properties

[11] The influence of the crater topography on mean and turbulence properties is first examined by comparing time series of 15 min averaged temperature, wind speed, turbulent kinetic energy, friction velocity, and heat flux measured at FLR (2 m level) and at SW (3 m level) for the entire experiment period when the data from both sites are available (Figure 2). The turbulent kinetic energy, or TKE, is calculated as [*Stull*, 1988]:

$$TKE = \frac{1}{2}\left(\overline{u'^2} + \overline{v'^2} + \overline{w'^2}\right), \quad (1)$$

and friction velocity is determined as

$$u_* = \left[\left(\overline{u'w'}\right)^2 + \left(\overline{v'w'}\right)^2\right]^{1/4}. \quad (2)$$

More rigorously, the contribution from the crosswind momentum flux to u_* is usually neglected and u_* is calculated simply from the streamwise component as $u_* = (-\overline{u'w'})^{-1/2}$. However, this becomes problematic at low wind speeds, a case often encountered within the crater, since on many occasions $\overline{u'w'}$ is positive. Thus the more robust equation (2) is used for the calculation of friction velocity.

[12] At both SW and FLR, all variables exhibit a strong diurnal cycle with higher values during daytime. In addition, there are large day-to-day variations at both sites during the 3 week period, with similar variations at the two sites caused by synoptic-scale forcing. In general, there is little difference between the two sites in daytime temperatures on windy days, suggesting that topographic effects on near-surface temperature are small in unstable or near-neutral conditions. Daily maximum temperatures are slightly (~0.5°C) higher and minimum temperatures are several degrees (1–5°C) lower at FLR than at SW. These differences may be attributed to crater sidewall heating or cooling and the smaller volume of air inside the crater compared to outside as defined by the topographic amplification factor [*Whiteman*, 1990]. The biggest temperature differences occur on clear, quiescent nights when FLR temperatures can be as much as 5–6°C colder than at SW, presumably a result of the formation of cold-air pools inside the crater caused by radiative cooling and cold air drainage [*Yao and Zhong*, 2009].

[13] Mean wind speeds at FLR are less than half those at SW during both daytime and nighttime regardless of ambient wind speed, suggesting that the crater atmosphere is sheltered from high background winds by the surrounding rim topography. Note that the difference in measurement heights underestimates the difference in wind speed between the two sites. The magnitudes of turbulent kinetic energy (TKE) and friction velocity (u_*) closely track the day-to-day variations of mean wind speeds. Friction velocity is larger at SW than at FLR, which is to be expected from the higher wind speeds at SW. As will be shown in section 3.2, which examines velocity covariances, the streamwise velocity covariance $\overline{u'w'}$, which is the dominant contributor to friction velocity, is generally larger outside the crater than inside.

[14] Unlike u_*, TKE inside the crater is often much larger than outside, with TKE values at FLR on windy days more than double the values at SW. The considerably larger TKE values at FLR, despite the much reduced mean wind speed, suggest that the crater topography acts to break down mean flow into turbulent motions. In other words, the crater, although small, is a powerful generator of turbulent motions. On 16–17 October, TKE reached peak values of 15 $m^2\ s^{-2}$, which is even greater than the peak TKE values measured at a fire-atmosphere interface during a grass fire [*Clements et al.*, 2008].

[15] No perceptible differences occurred between sensible heat fluxes at FLR and SW during daytime windy periods. During undisturbed nights with low winds outside the crater, which occurred most frequently in the last half of October,

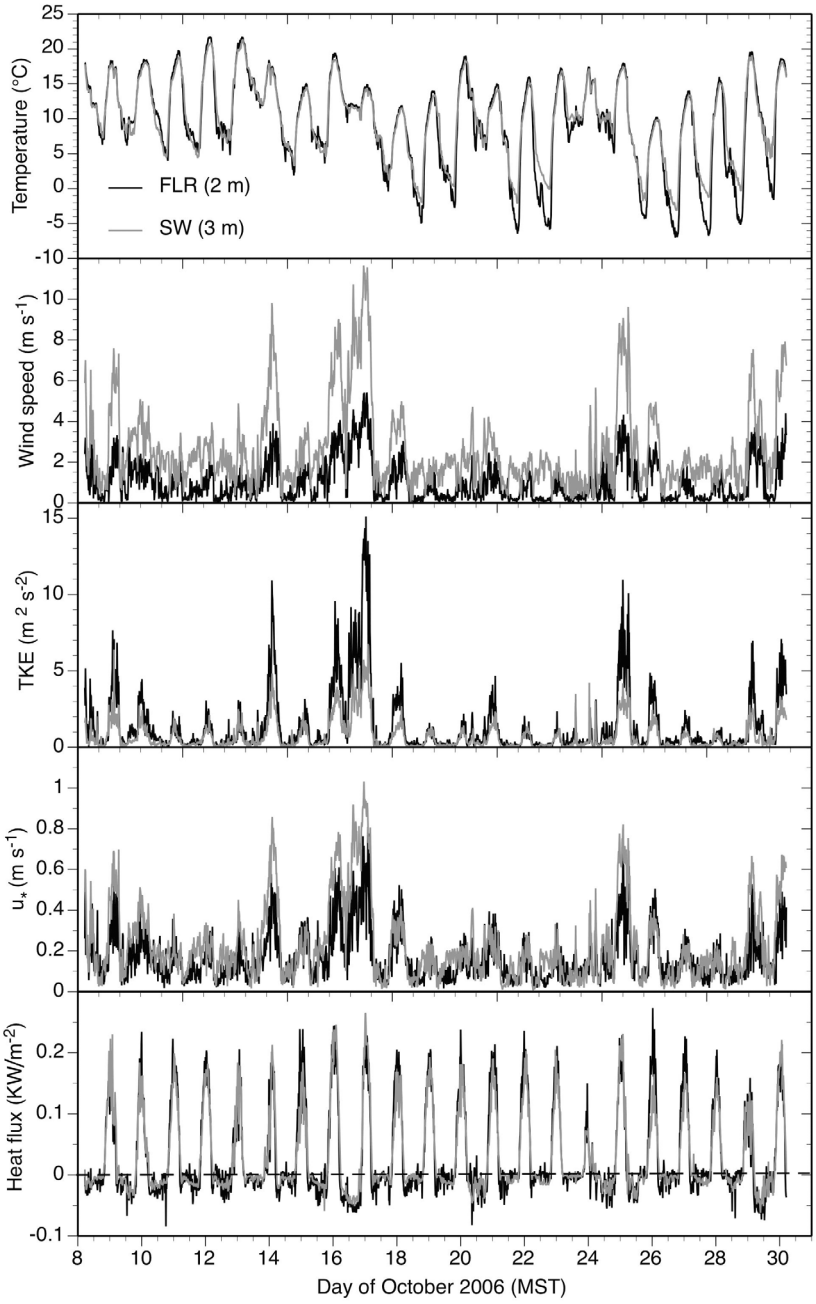

Figure 2. Time series of 15 min average temperature, wind speed, turbulence kinetic energy (TKE), frictional velocity (u_*), and vertical heat flux ($\rho c_p \overline{w'\theta'}$) for 9–30 October 2006.

shallow but strong temperature inversions formed on the floor of the crater [*Whiteman et al.*, 2008]. In these inversions, winds became calm and turbulent sensible heat flux at FLR became negligible. This illustrates the effects of strong ambient stability in suppressing downslope flows and forming quiescent conditions on the crater floor. On the other hand, when winds were strong at night, production of turbulence in the wake of the crater rim resulted in enhanced downward sensible heat flux within the crater compared to outside the crater.

[16] Figure 3 shows the temporal variation of the variances of the three velocity components, σ_u^2, σ_v^2 and σ_w^2, for the same data period. Velocity variances at all four levels inside the crater are larger than those outside the crater at 3 m, and increase with height, especially σ_w^2 on windy days. Also on windy days, σ_v^2 is more than 2 times larger inside the crater than outside, even near the ground at the 0.5 m level. The suggested explanation for these observations is that the turbulence in the crater is produced by eddies of topographic scale, which increase the velocity variance, especially in the transverse direction and produce mixing in the upper part of the crater. Although topographic eddies may significantly increase the turbulence within the crater when the background winds are strong, they do not significantly affect the

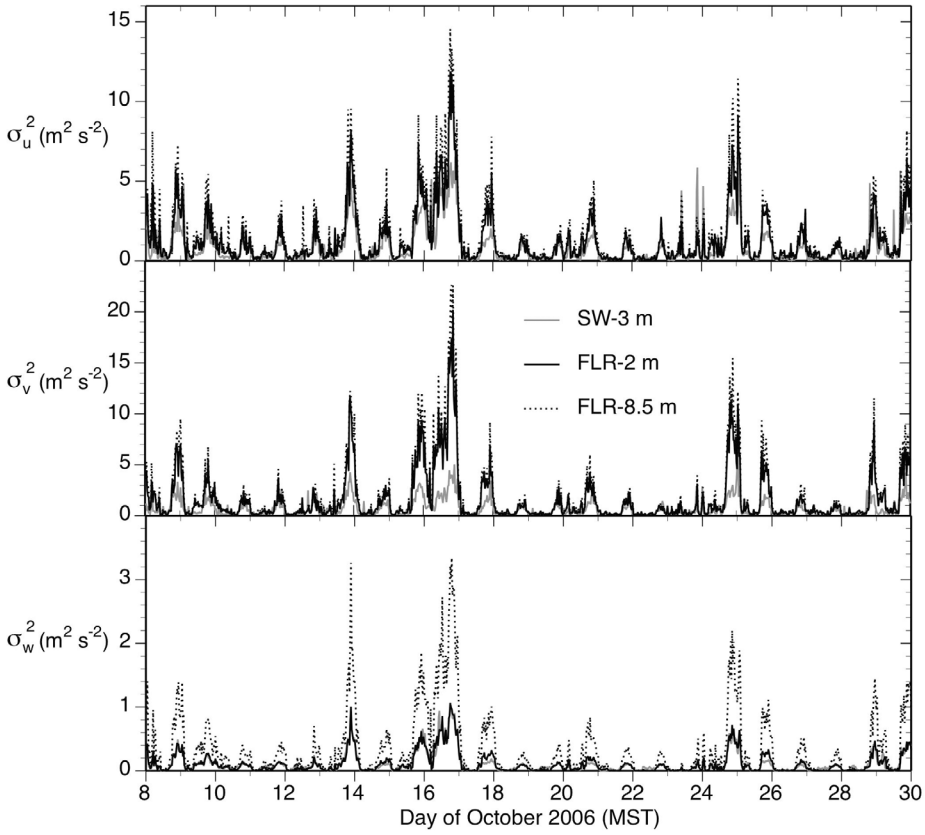

Figure 3. Same as Figure 2 but of 30 min averages for σ_u^2, σ_v^2, and σ_w^3.

surface momentum flux, which is dynamically correlated with the decreased wind speeds near the crater floor.

[17] To further understand the nature of the turbulence generated by the crater topography, we calculated power spectra of the square root of turbulent kinetic energy $TKE^{1/2}$ for the windiest 48 h period from 1700 MST on 15 October to 1700 MST on 17 October. Figure 4 shows the time averaged spectra for the SW and the FLR sites. As expected, a clear diurnal oscillation (1440 min) appears at both locations. Both sites also exhibit a semidiurnal signal (720 min). At shorter periods (~15 min or less), the power density is considerably higher at FLR than at SW. Given that the two sites mainly differ in topography, the increased energy at FLR in the shorter periods of the energy spectra is likely due to contributions from eddies generated by topography.

3.2. Velocity and Temperature Spectra

[18] Spectral density describes how energy of a variable is distributed over a range of different frequencies or eddy sizes. Previous studies [*Kaimal et al.*, 1972; *Caughey and Kaimal*, 1977; *Caughey et al.*, 1979] have shown a rather consistent behavior of spectral properties of turbulence over flat terrain. To understand the influence of the basin topography on turbulence properties, we compare various turbulence spectra observed inside and outside the crater. A Fast Fourier Transform (FFT) was used to compute velocity and temperature power spectra.

[19] The available data were divided into runs with N = 2^{16} data points, covering ~1 h (54.61 min) with a frequency range of 0.0003–10 Hz. Anemometer data were processed to align the x coordinate with the mean wind direction in each run, excluding runs with light winds ($u_* \leq 0.08$ m s^{-1}) and excessive wind direction variance ($a \tan \frac{\sqrt{\overline{v'^2}}}{\overline{u}} > 35°$). We will refer to this reduced data set as the "steady wind cases." There are ~246 runs for the SW site and a somewhat lower

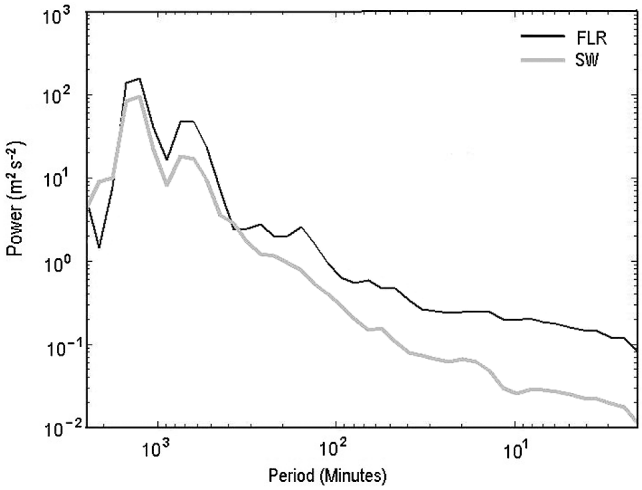

Figure 4. Global wavelet spectra of $TKE^{1/2}$ for the 48 h high-wind period between 1700 MST on 15 October and 1700 MST on 17 October 2006.

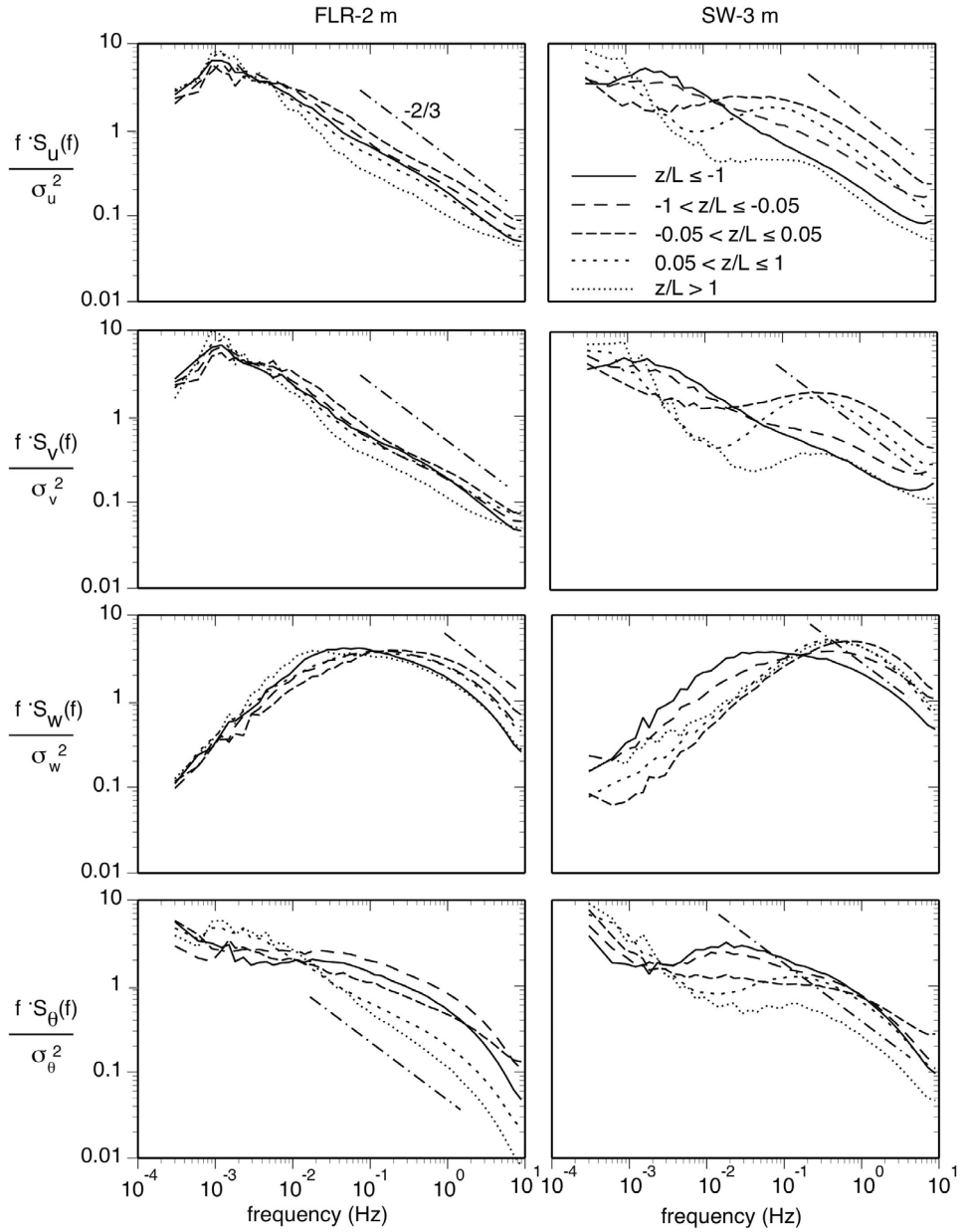

Figure 5. Averaged power spectra of *u*, *v*, *w*, and temperature for (left) 2 m at FLR and (right) 3 m at SW for very unstable ($z/L \leq -1.0$), unstable ($-1.0 < z/L \leq -0.05$), near- neutral ($-0.05 < z/L \leq 0.05$), stable ($0.05 < z/L \leq 1.0$), and very stable ($z/L > 1.0$) conditions for the steady wind cases.

number for the FLR site (171 runs at 2 m). The difference in the number of runs between SW and FLR is a result of lower wind speed, larger direction variance, and lower friction velocity in the crater (Figure 2).

[20] For each run, the stability is determined using the nondimensional variable $\frac{z}{L}$, with z being height above the ground and L the Obukhov length defined as

$$L = -\frac{u_*^3}{\kappa \frac{g}{\theta}\overline{\theta' w'}}, \tag{3}$$

where $\kappa = 0.4$ is the Von Karman constant and $\overline{\theta' w'}$ is the correlation of virtual potential temperature and vertical velocity fluctuations or buoyancy flux. The temperature measured by the sonic anemometers is to a good approximation equal to virtual potential temperature and is therefore used in the calculation. At SW, 91, 82, and 73 runs fall under the unstable ($\frac{z}{L} \leq -0.05$), neutral ($-0.05 < \frac{z}{L} < 0.05$), and stable ($\frac{z}{L} \geq 0.05$) categories, respectively; at FLR (2 m), the numbers for the three stability regimes are 83, 57, and 31. The apparent difference between the two sites in the percentage of runs falling under different stability regimes relative to the total number of runs is a direct result of the slightly different measurement heights at the two sites, as well as our data selection criteria. These criteria tend to exclude more stable cases at FLR when winds are lighter,

Table 2. Peak Frequencies of u, v, w, and T Spectra for the 3 m AGL Level of the SW Tower and the 2 m AGL Level of the FLR Tower in Different Stability Categories

	u (Hz)		v (Hz)		w (Hz)		T (Hz)	
Stability Category	SW	FLR	SW	FLR	SW	FLR	SW	FLR
Very unstable ($z/L < -1.0$)	0.002	0.001	0.002	0.001	0.06	0.06	0.02	0.001
Unstable ($-1.0 < z/L < -0.05$)	0.002	0.001	0.002	0.001	0.8	0.06	0.02	0.001
Neutral ($-0.05 < z/L < 0.05$)	0.06	0.001	0.06	0.001	0.8	0.1	0.02	0.001
Stable ($0.05 < z/L < 1.0$)	0.1	0.001	0.3	0.001	0.8	0.6	0.1	0.001
Very stable ($1.0 < z/L$)	0.2	0.001	0.3	0.001	0.8	0.6	0.1	0.001

directional variance is larger and frictional velocity is smaller.

[21] Figure 5 shows the averaged power spectra for the u, v, and w components of wind velocity and temperature at 3 m AGL at SW and at 2 m AGL at FLR in 5 stability categories: very unstable ($z/L < -1.0$), unstable ($-1.0 < z/L < -0.05$), neutral ($-0.05 < z/L < 0.05$), stable ($0.05 < z/L < 1.0$) and very stable ($1.0 < z/L$). A prominent feature of Figure 5 is that the velocity spectra at FLR vary little with stability class, while the velocity spectra at SW are very different for the different stability categories. The spectra are most similar at FLR and SW under unstable conditions. At SW, a double peak structure is found under neutral and stable conditions. This double peak structure illustrates the separate effects of small eddies and of mesoscale motions in the nocturnal boundary layer. At FLR, the topographically generated motions dominate the turbulence structure.

[22] Under very unstable and unstable conditions, the peak frequency at FLR for u and v components is around 0.001 Hz, but for the vertical wind component w and temperature the peak occurs at a higher frequency around 0.06 Hz. At SW, the peak frequency of the v spectra is higher than that of the u spectra under neutral and stable conditions, as described by *Kaimal et al.* [1972] for flat terrain. The spectral peak occurs at a lower frequency at FLR than at SW for temperature as well as for all three velocity components, especially for the v component where the peak at FLR (0.001 Hz) is two orders of magnitude lower than that at SW (0.3 Hz) in stable conditions (Table 2). Previous experiments over flat terrain found a shift of the spectral peak toward higher frequencies as stability increases. This occurs at SW. The inertial subrange of the energy spectra roughly follows a $-2/3$ slope (as shown) for all stability conditions, consistent with the Kolmogorov theory.

[23] These differences in the observed spectral properties between the two sites suggest a significant contribution of topographically generated eddies to the velocity spectra inside the crater. At FLR, a peak frequency between 0.001 Hz for the u and v components and an averaged velocity of 1.5 to 2 m s^{-1} corresponds to eddy sizes of 1000–2000 m, consistent with the 1200 m diameter of the crater. Outside the crater at SW the vertical fluctuations result mainly from surface-layer shear and buoyant production, but inside the crater eddies of crater scale also contribute to vertical fluctuations, thus lowering the peak frequency for w. The higher levels on the FLR tower feel a greater influence from the crater-generated eddies, and have correspondingly larger differences in spectral properties from those outside the crater at SW. The overall increase in energy in the frequency range of crater-size eddies is consistent with the much larger TKE values inside the crater (Figures 2 and 3). This, once again, suggests that the crater, which acts as a wind shelter with significantly reduced mean wind speed, converts some of the mean flow energy into turbulent motions.

[24] To investigate further the variation of spectra with height on the crater floor, we plot the averaged spectra at the 4 levels on the FLR tower for 3 stability categories (unstable $z/L < -0.05$, neutral $-0.05 < z/L < 0.05$, and stable $0.05 < z/L$) in Figure 6. Because the v spectra are like that of u (Figure 5), we only plot 3 components, u, w and temperature. Figure 6 shows that the spectra of u and temperature vary little with height, while the peak frequencies of the w spectra consistently move toward lower frequency with height. The temperature spectra are similar in shape to that of u spectra, but in unstable conditions the high-frequency range of the temperature spectra is also similar to that of vertical velocity component.

[25] *Panofsky and Dutton* [1984] described the spectral properties of turbulence over complex terrain. They noticed that the spectra of horizontal velocity components are spread over a large range of wavelengths, often with maximum energy at a scale of 1 km. These large eddies adjust slowly to changing terrain, causing the power spectra over nonuniform terrain to differ from that over uniform terrain. On the other hand, vertical velocity spectra over complex terrain have similar properties to those over uniform terrain, as demonstrated by the similarity between the w spectrum at SW and the 0.5 m level w spectrum at FLR. This is because the near-surface vertical velocity is dominated by small eddies that scale with measurement height and respond rapidly to changing terrain. But our results suggest that away from the ground surface, the turbulent eddies generated by the bowl-shaped basin contribute to the vertical velocity spectra at low frequencies, making the spectra differ from those outside the crater.

3.3. Covariances and Cospectra

[26] The covariances, or turbulent fluxes, quantify the transport of momentum and scalars by turbulent motions. Here, we examine the three velocity covariances or momentum fluxes ($\overline{u'w'}$, $\overline{v'w'}$ and $\overline{u'v'}$) and temperature and velocity covariances or heat fluxes ($\overline{w'\theta'}$, $\overline{u'\theta'}$ and $\overline{v'\theta'}$) at FLR and SW. Over flat terrain, the momentum and heat fluxes are often assumed to be roughly independent of height (i.e., change less than 10%) in the surface layer or lowest 10% of the boundary layer, and the mean profiles of velocity and temperature in this layer are assumed to be described by empirical formulas [*Businger et al.*, 1971; *Dyer*, 1974] based on MOST. Inside the crater, the assumption of horizontal homogeneity is violated and we expect that the fluxes and their cospectra will differ between the two sites.

[27] We consider the time series of 30 min averages of velocity covariances or momentum fluxes at each level of FLR and at SW on 16–17 October (Figure 7), a very windy period with near-neutral conditions ($-0.05 < z/L < 0.05$). At SW, $\overline{u'w'}$ is negative, indicating downward momentum

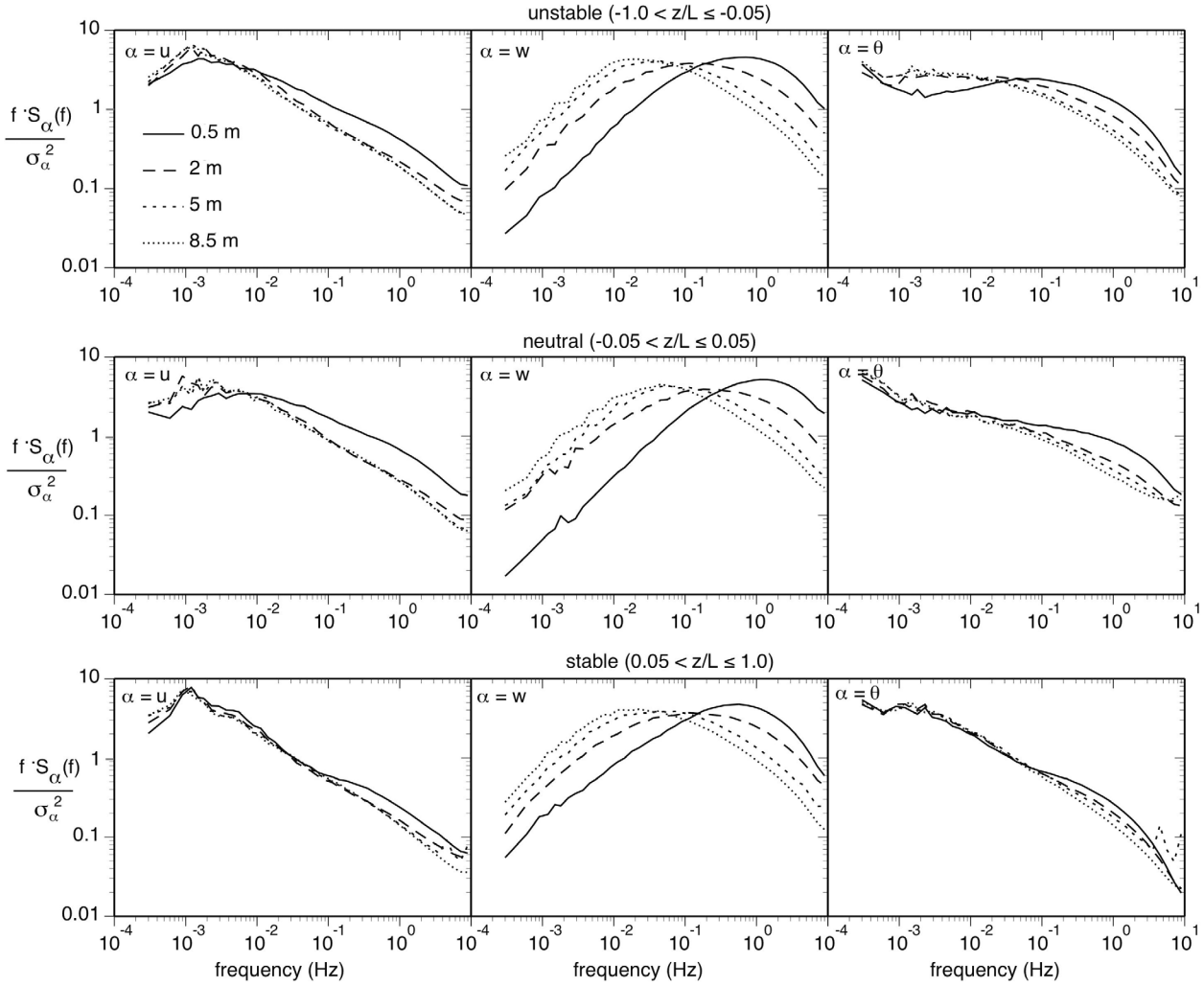

Figure 6. Averaged power spectra of u, w, and temperature at different levels of the FLR tower for unstable ($-1.0 < z/L \leq -0.05$), near- neutral ($-0.05 < z/L \leq 0.05$), and stable ($0.05 < z/L \leq 1.0$) conditions for the steady wind cases.

transport, as expected over flat terrain on windy days. At FLR, the values of $\overline{u'w'}$ at the first level above ground (0.5 m) are also negative with a time variation pattern similar to that of SW, but smaller in amplitude corresponding to smaller wind speeds at FLR. At higher levels, the values of $\overline{u'w'}$ begin to turn positive (nearly half are positive at 2 m, mostly positive at 5 m, and all positive at 8.5 m), indicating upward momentum transport. The change of sign in $\overline{u'w'}$, or the change of direction in momentum transport, between the lower and higher levels of FLR is one characteristic of turbulent transport of momentum in the crater.

[28] The change in sign of $\overline{u'w'}$, or the change in direction of momentum transport, can be explained by examining the budget for the streamwise momentum flux. Neglecting unmeasured terms involving horizontal gradients, $\overline{u'w'}$ is produced by the sum of shear production $-\overline{w'^2}\frac{\partial U}{\partial z}$, buoyancy production $\frac{g}{\Theta}\overline{u'\theta'}$, and turbulent transport $-\frac{\partial \overline{u'w'w'}}{\partial z}$ [*Wyngaard*, 2010]. Shear production of $\overline{u'w'}$ has a sign opposite to that of the local mean wind shear, implying gradient transfer of momentum and suggesting a change in sign of the velocity gradient above 2–5 m and thus a local maximum in the wind profile. However, a local wind maximum is observed on the crater floor only occasionally and at low wind speeds. The buoyancy term enhances downward momentum transport for negative horizontal heat flux and retards it for positive values, but is negligible for the near-neutral stratification of the windy period on 16–17 October. We find that the positive values observed for $\overline{u'w'}$ are produced by the turbulent transport term, which is generally positive above 2 m with an amplitude larger than shear production. The positive momentum flux transported down to the crater floor is produced in the upper layers of the crater flow. The ambient flow above the crater is from the southwest, while the flow on the crater floor is from the east (see Figure 13). Positive momentum flux is generated in the upper layers of the crater flow by shear opposite to that at the crater floor and transported down to the crater floor by the vigorous vertical turbulent mixing within the crater.

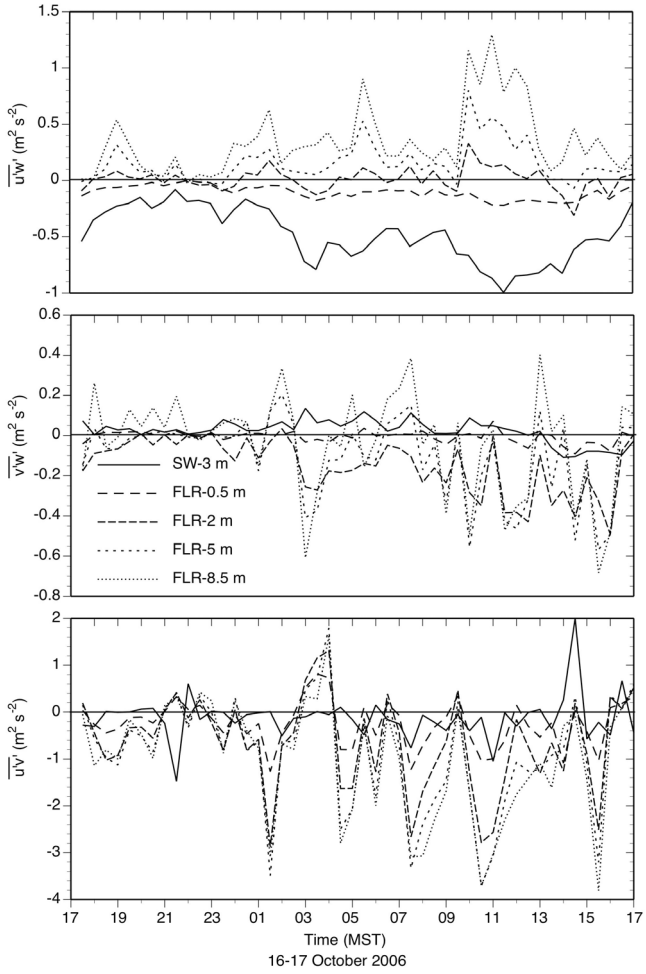

Figure 7. Momentum flux at various levels of the FLR tower and at 3 m at SW for the high-wind period of 1700 MST on 16 October to 1700 MST on 17 October 2006.

[29] The values of $\overline{v'w'}$ vary between −0.1 and 0.1 $m^2\ s^{-2}$ at SW and at the 0.5 m level of FLR during this windy period. The range of variation becomes larger (−0.7–0.5 $m^2\ s^{-2}$) at higher levels and the values are mostly negative. Similarly, for $\overline{u'v'}$, which represents the lateral transport of horizontal momentum, the pattern at SW is similar to that at 0.5 m at FLR. The values of $\overline{u'v'}$ increase with height at FLR, with values at 8.5 m being as much as 3 times the values at 0.5 m. The large exchange of horizontal momentum at the higher altitudes inside the crater is an outstanding feature of topographic eddies in the crater, mixing the air effectively during windy periods. The change of momentum fluxes with height at FLR indicates that the surface layer must be very shallow (less than 2 m) over the crater floor. Thus, one of the basic MOST assumptions, that of constant momentum flux, is not applicable to the crater except possibly for a shallow layer close to the floor.

[30] The time series of the three components of the heat flux, $\overline{u'\theta'}$, $\overline{v'\theta'}$ and $\overline{w'\theta'}$, are considered in Figure 8 during the same period as in Figure 7. At both FLR and SW, the vertical heat flux $\overline{w'\theta'}$ exhibits a strong diurnal cycle with relatively large upward (positive values) heat fluxes during the day and small downward (negative) fluxes at night. The temporal variations of $\overline{w'\theta'}$ are consistent among the four levels at FLR and are completely in phase with the time variations at SW. This result is not a surprise considering that the vertical heat flux is a strong function of surface heating and cooling. The two horizontal components of heat fluxes ($\overline{u'\theta'}$ and $\overline{v'\theta'}$) vary considerably among the four levels at FLR and between FLR and SW. Except for a brief period between 2200 and 2300 MST on 16 October, the $\overline{u'\theta'}$ values at SW are generally larger than at FLR, but the opposite is true for $\overline{v'\theta'}$, with consistently smaller values at SW than at FLR.

[31] The behavior of the two components of the horizontal heat flux can again be diagnosed by examining their turbulence budgets. Once more neglecting terms involving horizontal gradients, the horizontal heat flux $\overline{u_i'\theta'}$ (i = 1 and 2 for u and v, respectively) is produced by the sum of shear production, $-\overline{w'\theta'}\frac{dU_i}{dz}$, stratification production, $-\overline{u_i'w'}\frac{d\Theta}{dz}$, and turbulence transport $-\frac{\partial \overline{u_i'w'\theta'}}{\partial z}$. In the surface layer at SW, shear production and stratification production of the streamwise heat flux are both significant and have the same sign, so that $\overline{u_i'\theta'}$ is large and opposite in sign to the vertical heat flux. The cross wind heat flux at SW is negligible because $\frac{dV}{dz}$ and $\overline{v'w'}$ are both small. Within the crater, $\frac{dU}{dz}$ and $\overline{u'w'}$ are smaller than at SW, and the shear and stratification production terms for $\overline{u'\theta'}$ have opposite signs above 2 m because of the positive values for $\overline{u'w'}$. As a consequence, the streamwise heat flux is much smaller on the crater floor than at SW. The crosswind heat flux budget is dominated by turbulent transport, which is highly variable so that $\overline{v'\theta'}$ is also small on the crater floor, although being somewhat larger than at SW.

[32] Over uniform, flat terrain, the vertical heat flux component ($\overline{w'\theta'}$) is smaller than the horizontal heat flux components ($\overline{u'\theta'}$ and $\overline{v'\theta'}$), but vertical gradients of heat flux are likely much larger than horizontal gradients, making horizontal heat flux divergences negligible compared to vertical flux divergences. Inside the small crater, horizontal gradients of heat flux may not be negligible and may be comparable to vertical gradients except very near the surface and, as a result, horizontal heat flux divergence may also contribute to the heat budget of the crater boundary layer.

[33] Figure 9 compares the 30 min averages of momentum flux components, friction velocity, and kinematic vertical heat flux at the 0.5 m level of the FLR tower with fluxes at the 2, 5 and 8.5 m levels of the same tower for the steady wind cases. The vertical heat flux in the crater remains almost constant with height, while the momentum flux and friction velocity vary significantly with height. These results provide further evidence for the conclusion that the surface layer or the constant flux layer is very shallow (<2 m) in the crater. The results also reveal that the constant flux layer is slightly higher for heat flux than for momentum flux.

[34] To further understand the behavior of the covariances and their differences between SW and FLR, we analyze the cospectrum defined as [*Stull*, 1988, p. 330]

$$Co_{uw}(f) = F_{ur}(f) \cdot F_{wr}(f) + F_{ui}(f) \cdot F_{wi}(f), \qquad (4)$$

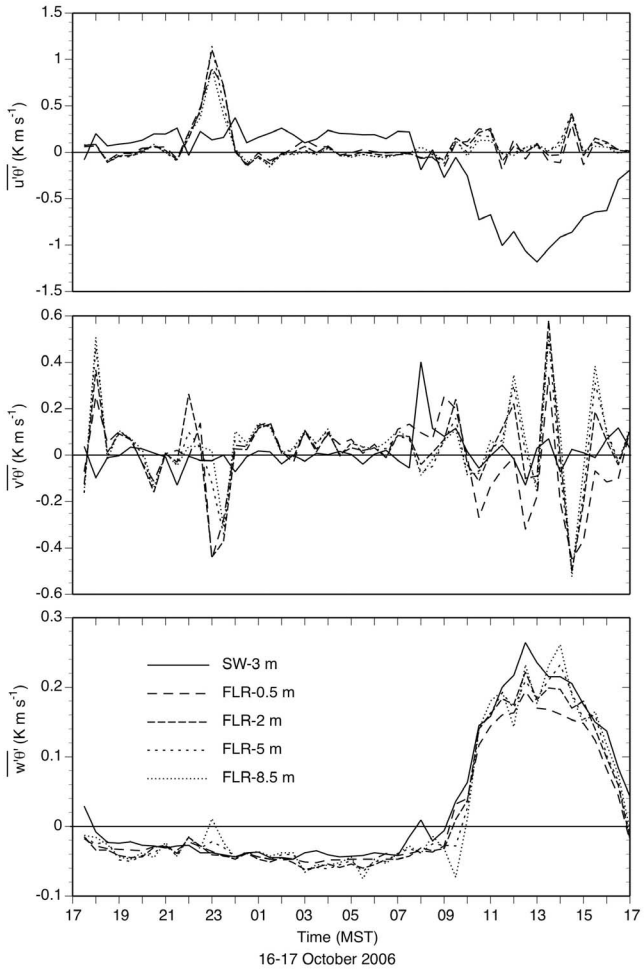

Figure 8. Similar to Figure 7 but for heat flux.

and the phase spectrum defined by

$$\phi_{uw}(f) = \arctan\left\{\frac{F_{ui}(f)\cdot F_{wr}(f) - F_{ur}(f)\cdot F_{wi}(f)}{Co}\right\}, \quad (5)$$

where F_{ur} and F_{ui} are the real and imaginary parts of the discrete Fourier transform of u', and F_{wr} and F_{wi} are the real and imaginary parts of the discrete Fourier transform of w'. When considering $\overline{w'\theta'}$, θ is substituted for u. The co-spectrum indicates the contributions of different frequencies of eddy motions to the turbulent fluxes or covariances, while the phase spectrum indicates the phase relation between the two quantities u' and w', or θ' and w', in the covariances; differences of phase shift usually mean that motions are forced by different mechanisms. For example, for buoyancy waves, θ' and w' are typically 90 or 270 degrees out of phase, while for turbulent motions, they are either in phase (0 degrees) or completely out of phase (180 degrees) [*Stull*, 1988, p. 332]. To also show the dependence on phase angle, the cospectral amplitudes are sorted into four subranges of the phase angle: −45 to 45, 45 to 135, 135 to −135 and −135 to −45 degrees.

[35] Figure 10 shows the averaged spectral plot of the variations of normalized cospectra $\frac{Co_{uw}(f)}{|\overline{u'w'}|}$ with frequency for each level of FLR and for SW for 3 stability categories using all available data. The average cospectrum for each subrange represents 0, 90, 180 or 270 degrees in phase lag. The ratio $\frac{Co_{uw}(f)}{|\overline{u'w'}|}$ denotes the percentage contribution of different frequencies to the $\overline{u'w'}$ covariance. Several features emerge from a careful examination of these plots. First, at all four levels of FLR and at SW, all four phase lags appear in the average cospectra, but the 0 degree or the 180 degree phase lags are dominant. Second, the 180 degree phase lag dominates at SW and at the 0.5 m level of FLR in all 3 stabilities. But, with an increase in height at FLR, the 0 degree phase lag gradually takes over and becomes dominant at the 8.5 m level. This is consistent with the fact that $\overline{u'w'}$ values are always negative at 0.5 m, and become all positive at 8.5 m, as shown in Figure 7. Third, the peak frequency of dominant cospectra is 0.05–0.1 Hz at SW and 0.2–0.8 Hz at the 0.5 m level of FLR, moving toward lower frequency as height increases (near 0.05 Hz at 2 m and 0.01 Hz at 5 and 8.5 m). Finally, the distribution of cospectra at SW and at the 0.5 m level at FLR is very similar in unstable and neutral conditions, and the distribution at the rest of the FLR levels shares similar patterns.

[36] The averaged normalized cospectra for heat flux $\frac{Co_{w\theta}(f)}{|\overline{w'\theta'}|}$ are shown in Figure 11 for 3 stability categories. Similar to the momentum fluxes, the distribution at SW resembles that at the 0.5 m level at FLR. In stable conditions, the distribution is dominated by the 180 degree phase lag, indicating downward heat flux. The peak frequency associated with the 180 degree phase lag occurs at frequencies of 0.06–0.3 Hz at SW and 0.2 Hz at the 0.5 m level of FLR, shifting to lower frequencies with increasing height (0.01–0.02 Hz at 2, 5 and 8.5 m). The cospectra corresponding to 90 and 270 degree phase lag overlap and have a small peak at about 0.6 Hz in stable conditions. This weak 0.6 Hz peak coincides with a local minimum in the 180 degree and 0 degree phase lag at 2, 5 and 8.5 m levels. This phenomenon appears to be a constant feature since it can also be seen on individual nights, although as the wind weakens the peak moves slightly toward lower frequencies. It is not entirely clear what may have caused this maximum of the 90 and 270 degree phase lag. Since it appears only at night, it is possible that this phenomenon is the result of interactions between turbulent motions and buoyancy oscillations under stable stratification. During daytime when the atmosphere is unstable, the heat flux is upward, so that cospectra corresponding to 0 degree phase lag are the largest, with the peak frequency also at 0.06 Hz at SW and 0.2 Hz at the 0.5 m level at FLR, but with 0.01 Hz at 2, 5 and 8.5 m.

3.4. Standard Deviations of Velocity

[37] MOST has been widely adopted as the basis for treatment of the surface layer in many atmospheric models and these models are widely used for environmental prediction both over flat and complex terrain. It has been tested in several boundary layer experiments (e.g., the Kansas experiment [*Businger et al.*, 1971], the International Turbulence Comparison Experiment [*Dyer and Bradley*, 1982], etc.). The MOST approach was established over homogeneous terrain under stationary conditions, and it has been used successfully in many applications. There are numerous MOST-based formulas and here, as an example, we compare the normalized

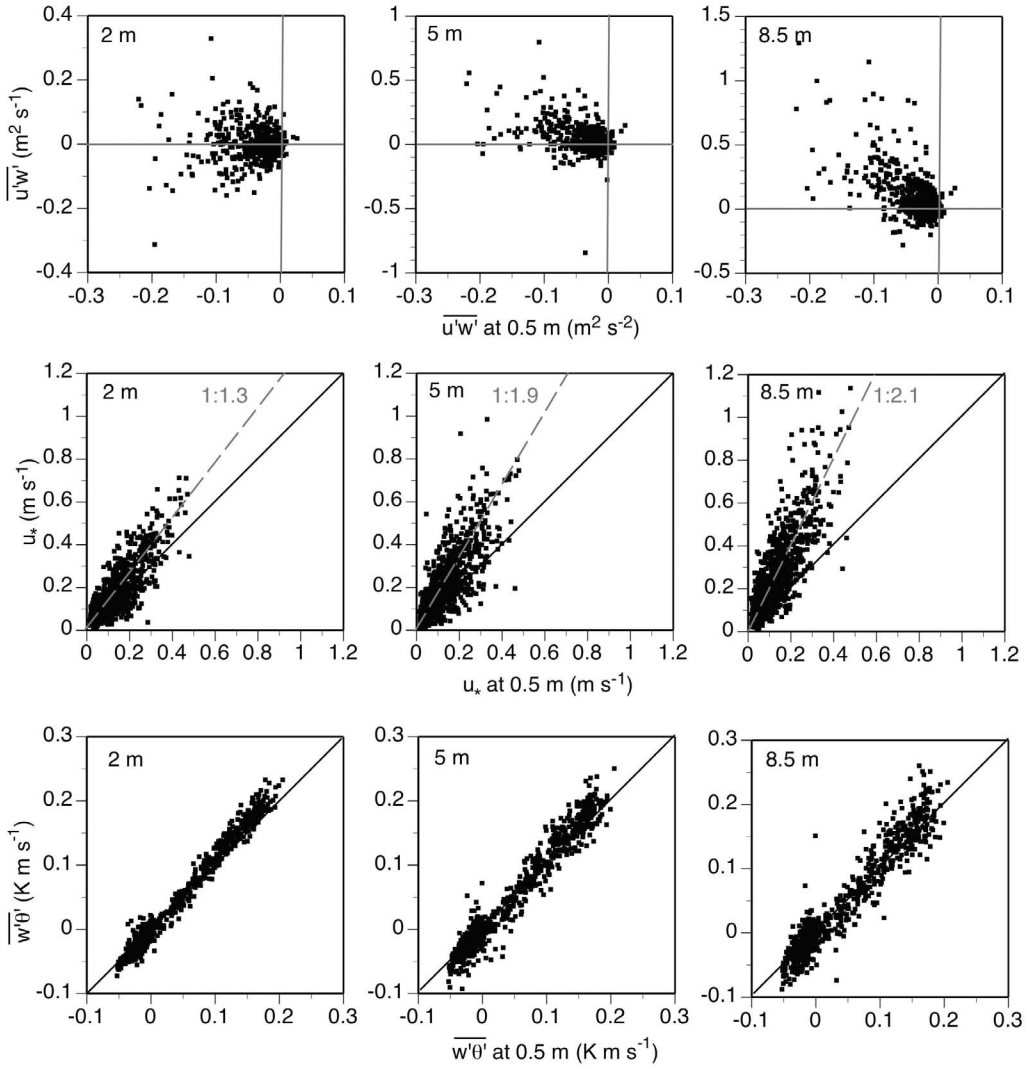

Figure 9. Comparison of momentum flux, friction velocity, and kinematic vertical heat flux at different levels of the FLR tower for the steady wind cases.

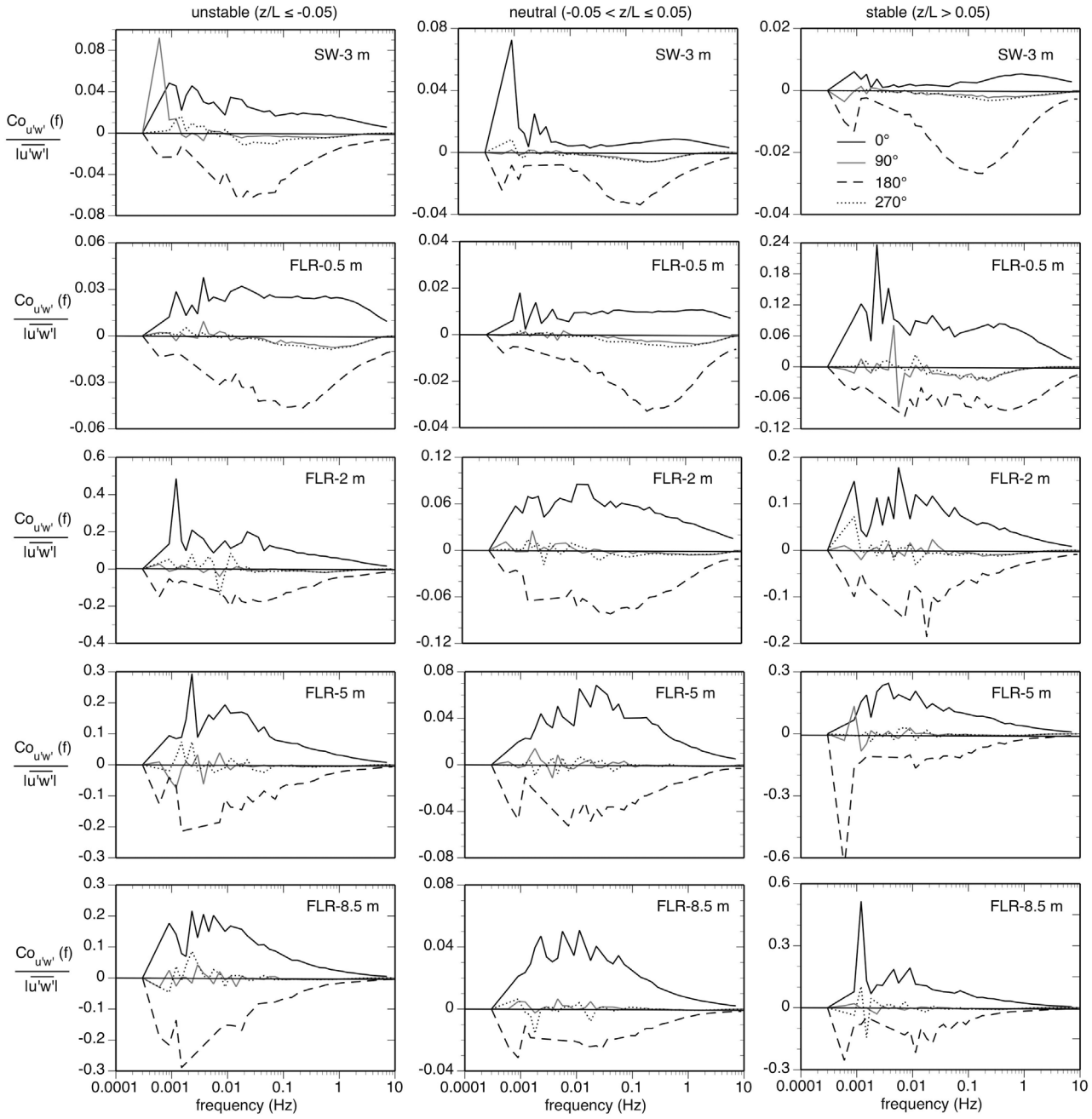

Figure 10. Averaged normalized velocity cospectra and phase spectra at various levels of the FLR tower and at 3 m at SW for unstable ($z/L \leq -0.05$), near-neutral ($-0.05 < z/L \leq 0.05$), and stable ($z/L > 0.05$) conditions for the steady wind cases.

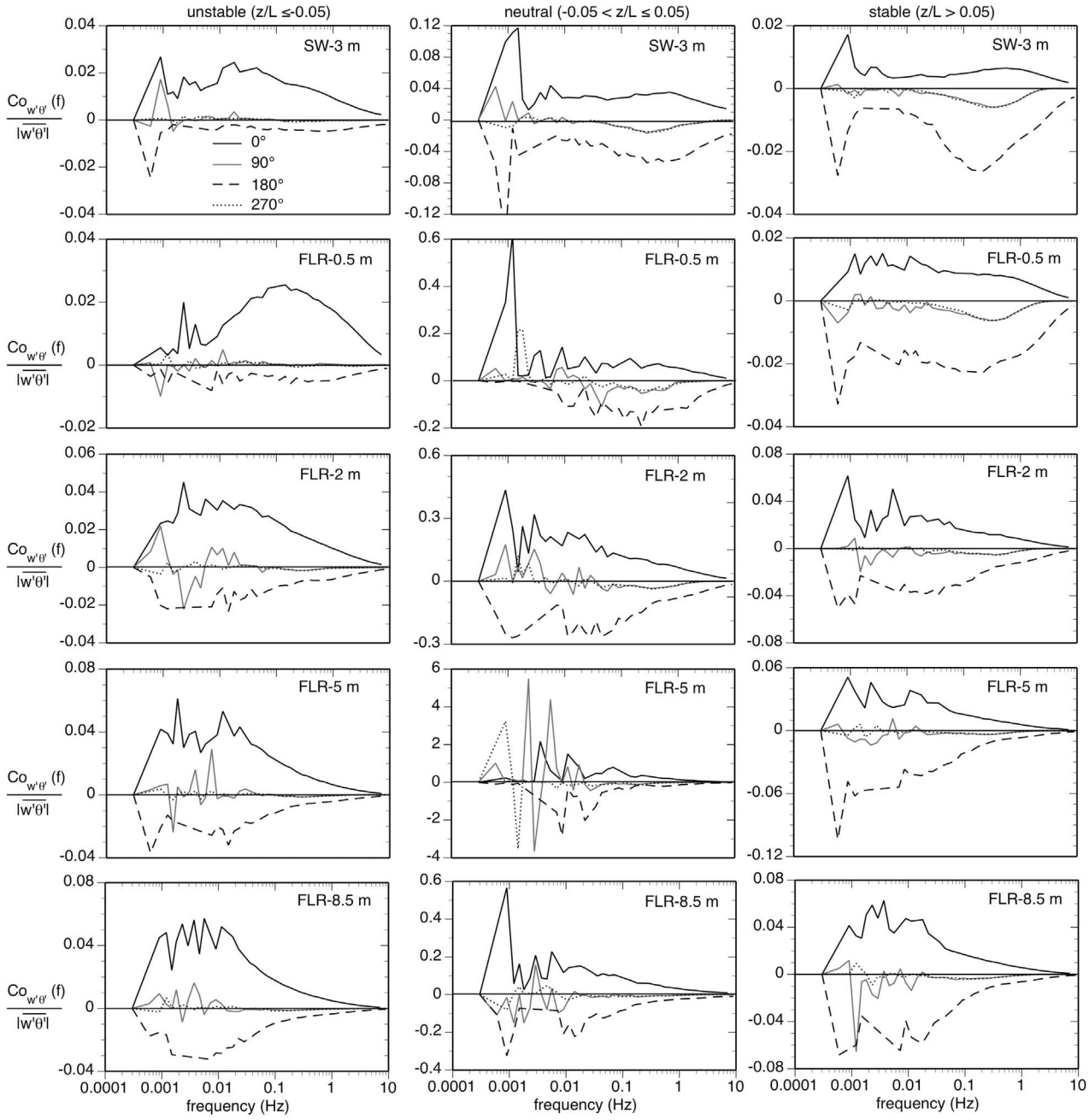

Figure 11. Same as Figure 10 but for normalized heat flux cospectra and phase spectra.

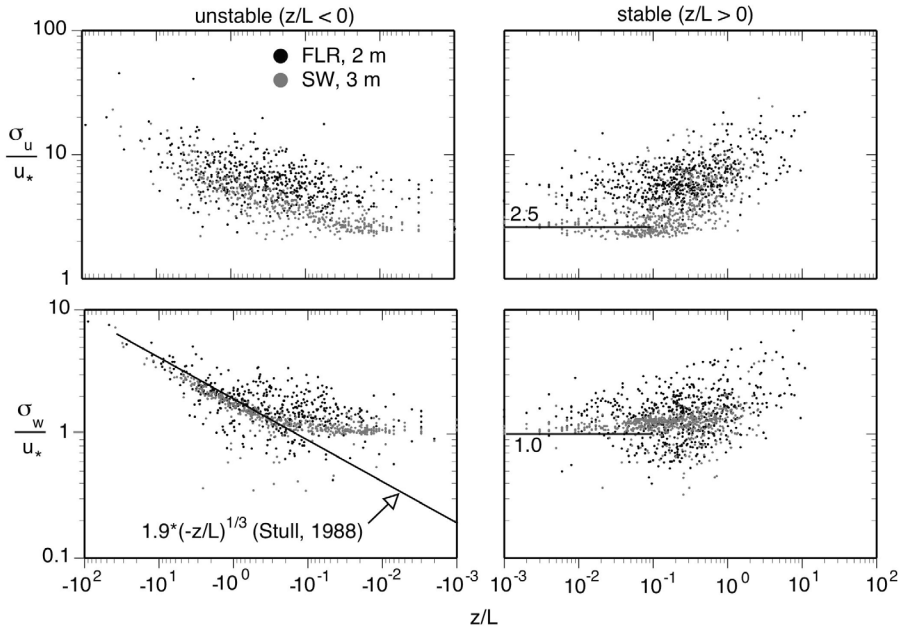

Figure 12. Normalized standard deviations of u and w components versus stability parameter for (left) unstable and (right) stable conditions for the steady wind cases. The lines, $\frac{\sigma_u}{u_*} = 2.5$ and $\frac{\sigma_w}{u_*} = 1.0$, correspond to values over flat terrain for neutral conditions [*Stull*, 1988].

standard deviation of u and w components at the 2 m level at FLR and at the 3 m level at SW versus stability parameter with the results from *Stull* [1988] obtained over flat terrain (Figure 12). Note that the left-hand column in Figure 12 is for unstable stratification and right-hand column is for stable stratification. In neutral conditions, $\frac{\sigma_u}{u_*} = 4.0$ and 9.0 for FLR and SW, respectively, which are higher than values obtained by Stull ($\frac{\sigma_u}{u_*} = 2.5$). σ_u shows more scatters at FLR than at SW. The distribution of σ_w from SW data is closer to Stull's formulas for unstable [$\frac{\sigma_w}{u_*} = 1.9 * (-z/L)^{1/3}$], neutral ($\frac{\sigma_w}{u_*} = 1.0$) and stable ($\frac{\sigma_w}{u_*} = 1.58$) [*Stull*, 1988]. The data from FLR scatter more widely, but follow similar trends.

4. Conclusions

[38] Turbulence data collected using flux towers inside and outside Arizona's Meteor Crater are analyzed to determine the influence of basin topography on turbulence properties, focusing particularly on windy conditions.

[39] Similar to that over flat terrain, vertical velocity spectra inside the crater show a shift of the spectral peak toward higher frequencies as stability changes from unstable to stable, but spectra of horizontal velocity are nearly invariant with stability. Some aspects of turbulent properties inside the crater are found to be considerably different from those over flat terrain, especially under stable and near-neutral conditions. Unlike over flat terrain where the spectral peaks for the u and v components occur at different frequencies with the peak frequency for v an order of magnitude higher, inside the crater the peak frequency for v is significantly lower and is usually comparable to the peak frequency of the u spectrum. Similarly, the peak frequencies for w and temperature are also lower inside the crater than outside. Another important finding is that turbulent momentum flux and friction velocity vary with height, indicating that the assumption of a constant flux layer, as often assumed for the surface layer over flat terrain, is no longer valid within the crater except for a very shallow layer (<2 m) over the crater floor. Consequently, the MOST-based empirical formulae may not be useful for describing the properties of the surface layer over the crater floor.

[40] Perhaps the most important observation is that the turbulence level in the crater is significantly higher on windy days than that on the adjacent plain. The results show that while the mean wind speed inside the crater is consistently lower (less than half) at the crater floor than outside, the turbulent kinetic energy on windy days more than doubles that outside during both day and night. Spectral

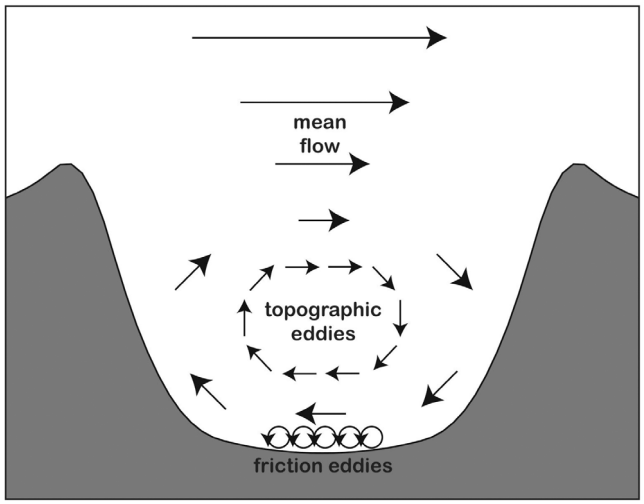

Figure 13. Conceptual plot for the turbulence generation in the crater.

analysis shows that these eddies are of the scale of the crater and thus are likely generated by the crater topography. In other words, the crater, although small, is efficiently sheltered from mean winds outside the crater, but is a powerful generator of topographic turbulent motions (see conceptual sketch in Figure 13). On windy days (mean surface wind > 10 m s^{-1}), 15 min averaged TKE on the crater floor may reach a value of 15 m^2 s^{-2}. This result can have important implications for applications such as wind energy, agriculture, and air pollution dispersion.

[41] **Acknowledgments.** This material is based on work supported by the National Science Foundation under grants ATM 0837860 and ATM 0837870. Any opinions, findings, conclusions, or recommendations expressed are those of the authors and do not necessarily reflect the views of the National Science Foundation. P. Fu, who worked on the paper while on sabbatical leave from Lanzhou University, is partly supported by the National Science Foundation of China under grant 40633017. P. Fu wishes to thank J. Huang from Lanzhou University for his support. We thank the Barringer Crater Company and Meteor Crater Enterprises, Inc., for access to the Meteor Crater and the National Center for Atmospheric Research Earth Observing Laboratory (EOL) for providing equipment, field support, and quality-controlled data sets. Steve Oncley, Bill Brown, and Gordon Maclean from EOL are especially thanked for their valuable field and data processing assistance. S. W. Hoch provided Figure 1, and M. T. Kiefer helped with Figure 13. The data processing and analysis were performed on supercomputers managed and operated by the Computational and Information Systems Laboratory at the National Center for Atmospheric Research.

References

Businger, J. A., J. C. Wyngaard, Y. Izumi, and E. F. Bradley (1971), Flux-profile relationships in the atmospheric surface layer, *J. Atmos. Sci.*, *28*, 181–189, doi:10.1175/1520-0469(1971)028<0181:FPRITA>2.0.CO;2.

Caughey, S. J., and J. C. Kaimal (1977), Vertical heat flux in the convective boundary layer, *Q. J. R. Meteorol. Soc.*, *103*, 811–815, doi:10.1002/qj.49710343821.

Caughey, S. J., J. C. Wyngaard, and J. C. Kaimal (1979), Turbulence in the evolving stable boundary layer, *J. Atmos. Sci.*, *36*, 1941–1052.

Clements, C. B., S. Zhong, X. Bian, and W. Heilman (2008), Observations of turbulence during grass fires, *J. Geophys. Res.*, *113*, D22102, doi:10.1029/2008JD010014.

Coulter, R. L., and J. C. Doran (2002), Spatial and temporal occurrences of intermittent turbulence during CASES-99, *Boundary Layer Meteorol.*, *105*, 329–349, doi:10.1023/A:1019993703820.

Dyer, A. J. (1974), A review of flux-profile relations, *Boundary Layer Meteorol.*, *7*, 363–372, doi:10.1007/BF00240838.

Dyer, A. J., and E. F. Bradley (1982), An alternative analysis of flux-gradient relationships at the 1976 ITCE, *Boundary-Layer Meteorol.*, *22*, 3–19.

Horst, T., and J. Doran (1988), The turbulence structure of nocturnal slope flow, *J. Atmos. Sci.*, *45*, 605–616, doi:10.1175/1520-0469(1988)045<0605:TTSONS>2.0.CO;2.

Kaimal, J. C., and J. J. Finnigan (1994), *Atmospheric Boundary Layer Flows: Their Structure and Measurement*, 289 pp., Oxford Univ. Press, New York.

Kaimal, J. C., J. C. Wyngaard, Y. Izumi, and O. R. Cote (1972), Spectral characteristics of surface-layer turbulence, *Q. J. R. Meteorol. Soc.*, *98*, 563–589, doi:10.1002/qj.49709841707.

Kaimal, J. C., R. A. Eversole, D. H. Lenschow, B. B. Stankov, P. H. Kahn, and J. A. Businger (1982), Spectral characteristics of the convective boundary layer over uneven terrain, *J. Atmos. Sci.*, *39*, 1098–1114.

Kolmogorov, A. N. (1941), The local structure of turbulence in incompressible viscous fluid for very large Reynolds number, *Dokl. Akad. Nauk SSSR*, *30*, 301–303.

Mahrt, L., J. Sun, W. Blumen, T. Delany, and S. Oncley (1998), Nocturnal boundary layer regimes, *Boundary Layer Meteorol.*, *88*, 255–278, doi:10.1023/A:1001171313493.

Martins, C. A., O. L. L. Moraes, O. C. Acevedo, and G. A. Degrazia (2009), Turbulence intensity parameters over a very complex terrain, *Boundary Layer Meteorol.*, *133*, 35–45, doi:10.1007/s10546-009-9413-3.

Mengesha, Y. G., P. A. Taylor, and D. H. Lenschow (2001), Boundary-layer turbulence over the Nebraska sandhills, *Boundary Layer Meteorol.*, *100*, 3–46, doi:10.1023/A:1018987113076.

Monin, A. S., and A. M. Obukhov (1954), Basic laws of turbulent mixing in the ground layer of the atmosphere, *Trudy Geofiz. Inst. Akad. Nauk SSSR*, *24*, 163–187.

Monti, P., H. J. S. Fernando, M. Princevac, W. C. Chan, T. A. Kowalewski, and E. R. Pardyjak (2002), Observations of flow and turbulence in the nocturnal boundary layer over a slope, *J. Atmos. Sci.*, *59*, 2513–2534, doi:10.1175/1520-0469(2002)059<2513:OOFATI>2.0.CO;2.

Nieuwstadt, F. T. M. (1984), The turbulence structure of the stable nocturnal boundary layer, *J. Atmos. Sci.*, *41*, 2202–2216, doi:10.1175/1520-0469(1984)041<2202:TTSOTS>2.0.CO;2.

Panofsky, H. A., and J. A. Dutton (1984), *Atmospheric Turbulence*, John Wiley, New York.

Princevac, M., J. C. R. Hunt, and H. J. S. Fernando (2008), Quasi-steady katabatic winds on slopes in wide valleys: Hydraulic theory and observations, *J. Atmos. Sci.*, *65*, 627–643, doi:10.1175/2007JAS2110.1.

Rotach, M. W., et al. (2004), Turbulence structure and exchange processes in an Alpine valley: The Riviera Project, *Bull. Am. Meteorol. Soc.*, *85*, 1367–1385, doi:10.1175/BAMS-85-9-1367.

Sorbjan, Z. (1986), On similarity in the atmospheric boundary layer, *Boundary Layer Meteorol.*, *34*, 377–397, doi:10.1007/BF00120989.

Stull, R. (1988), *An Introduction to Boundary Layer Meteorology*, Kluwer Acad., Norwell, Mass.

Whiteman, C. D. (1990), Observations of thermally developed wind systems in mountainous terrain, in *Atmospheric Processes Over Complex Terrain*, *Meteorol. Monogr.*, vol. 23, no. 45, edited by W. Blumen, chap. 2, pp. 5–42, Am. Meteorol. Soc., Boston, Mass.

Whiteman, C. D., and S. Zhong (2008), Downslope flows on a low-angle slope and their interactions with valley inversions. part I: Observations, *J. Appl. Meteorol. Climatol.*, *47*, 2023–2038, doi:10.1175/2007JAMC1669.1.

Whiteman, C. D., et al. (2008), METCRAX (2006)—Meteorological Experiments in Arizona's Meteor Crater, *Bull. Am. Meteorol. Soc.*, *89*, 1665–1680, doi:10.1175/2008BAMS2574.1.

Wilczak, J. M., S. P. Oncley, and S. A. Stage (2001), Sonic anemometer tilt correction algorithms, *Boundary Layer Meteorol.*, *99*, 127–150, doi:10.1023/A:1018966204465.

Wyngaard, J. C. (2010), *Turbulence in the Atmosphere*, 393 pp., Cambridge Univ. Press, New York.

Wyngaard, J. C., and O. R. Coté (1971), The budgets of turbulent kinetic energy and temperature variance in the atmospheric surface layer, *J. Atmos. Sci.*, *28*, 190–201, doi:10.1175/1520-0469(1971)028<0190:TBOTKE>2.0.CO;2.

Yao, W., and S. Zhong (2009), Nocturnal temperature inversions in a small, enclosed basin and their relationship to ambient atmospheric conditions, *Meteorol. Atmos. Phys.*, *103*, 195–210, doi:10.1007/s00703-008-0341-4.

X. Bian, Northern Research Station, U.S. Department of Agriculture Forest Service, East Lansing, MI, USA.

P. Fu, College of Atmospheric Sciences, Lanzhou University, Lanzhou City 730000, China. (fupj@lzu.edu.cn)

T. Horst, National Center for Atmospheric Research, Boulder, CO, USA.

C. D. Whiteman, Department of Atmospheric Sciences, University of Utah, Salt Lake City, UT, USA.

S. Zhong, Department of Geography, Michigan State University, East Lansing, MI, USA.